

Zinc-induced oligomerisation of zinc α 2 glycoprotein reveals multiple fatty acid binding sites

Henna Zahid*†‡, Layeque Miah*†, Andy M. Lau†‡, Lea Brochard‡, Debolina Hati†, Tam T. T. Bui[§], Alex F. Drake[§], Jayesh Gor‡, Stephen J. Perkins‡ and Lindsay C. McDermott†‡||

* These two authors contributed substantially to this work.

† Diabetes and Nutritional Sciences Division, Franklin Wilkins Building, 150 Stamford Street, King's College London, London SE1 9NH, U. K.

‡ Department of Structural and Molecular Biology, University College London, Darwin Building, Gower Street, London WC1E 6BT, UK

§ Biomolecular Spectroscopy Centre, Optical and Chiroptical Spectroscopy Facility, The Wolfson Wing, Hodgkin Building, King's College London, London SE1 1UL, U. K.

|| To whom correspondence should be addressed (Department of Structural and Molecular Biology, University College London, Darwin Building, Gower Street, London WC1E 6BT, UK. Tel: 020 7679 7048; Fax: 020 7679 7193; e-mail: l.mcdermott@ucl.ac.uk)

Running title: Zinc-induced oligomerisation of zinc α 2 glycoprotein

Key words: Zinc- α 2-glycoprotein; obesity; oligomerisation; analytical ultracentrifugation; fluorescence; fatty acids.

Abbreviations: Analytical ultracentrifugation (AUC); Dynamic light scattering (DLS); Zinc α 2 glycoprotein (ZAG)

Abstract (250 words) (Background, aims, results, conclusions)

Zinc $\alpha 2$ glycoprotein (ZAG) is an adipokine with a class I major histocompatibility complex protein fold and is associated with obesity and diabetes. Although its intrinsic ligand remains unknown, ZAG binds the dansylated C_{11} fatty acid, DAUDA, in the groove between the $\alpha 1$ and $\alpha 2$ domains. The surface of ZAG has about 15 weak zinc binding sites deemed responsible for precipitation from human plasma. Here the functional significance of these metal sites was investigated. Analytical ultracentrifugation and circular dichroism showed that zinc, but not other divalent metals, cause ZAG to oligomerise in solution. Thus ZAG dimers and trimers were observed in the presence of 1 mM and 2 mM zinc. Molecular modelling of X-ray scattering curves and sedimentation coefficients indicated a progressive stacking of ZAG monomers, suggesting the ZAG groove may be occluded in these. Using fluorescence-detected sedimentation velocity, these ZAG-zinc oligomers were again observed in the presence of the fluorescent boron dipyrromethene fatty acid C_{16} -BODIPY. Fluorescence spectroscopy confirmed that ZAG binds C_{16} -BODIPY. ZAG binding to C_{16} -BODIPY, but not to DAUDA, was reduced by increased zinc concentrations. We conclude that the lipid binding groove in ZAG contains at least two distinct fatty acid binding sites for DAUDA and C_{16} -BODIPY, similar to the multiple lipid binding seen in the structurally-related immune protein Cd1c. In addition, because high concentrations of zinc occur in the pancreas, the perturbation of these multiple lipid binding sites by zinc may be significant in Type 2 diabetes where dysregulation of ZAG and zinc homeostasis occurs. (247 words)

Summary statement (40 words): Zinc causes the adipokine and class I MHC-like protein, zinc $\alpha 2$ glycoprotein (ZAG), to oligomerize in solution. Our experiments reveal the presence of two distinct fatty acid binding sites within ZAG, of which one is abrogated by oligomer formation. (39 words)

INTRODUCTION

In 2014, the global presence of diabetes was estimated to be 9% among adults [1]. Diabetes is associated with obesity and increases the risk of heart disease, stroke, blindness and kidney failure. If untreated, the World Health Organisation predicts that diabetes will be the seventh leading cause of death in 2030 [1]. The plasma protein zinc- α 2-glycoprotein (ZAG) has been associated with type 2 diabetes. ZAG was first isolated from human plasma in 1961 by precipitation with zinc salts [2]. ZAG is expressed in the pancreas [3] and secreted from adipocytes, defining it as an adipokine [4]. The expression of ZAG in adipocytes is inversely associated with body fat mass [5, 6]. Indeed subcutaneous white fat from type 2 diabetic patients shows reduced expression of ZAG compared with healthy control patients [7, 8]. ZAG is upregulated in urine from diabetic patients [9, 10] and contains a non-synonymous single nucleotide polymorphism rs4215 associated with obesity [11, 12]. ZAG also participates in lipolysis and the control of body fat mass [5, 13]; treatment of ob / ob mice with ZAG resulted in an increase in pancreatic insulin and a reduction in plasma glucose [14]. Meanwhile incubation of human primary skeletal muscle with ZAG caused an increase in the expression of glucose transporter type 4 and activation of AMPK, a regulator of energy metabolism [15]. Despite these cellular observations, the molecular function of ZAG has remained elusive. Determining the molecular mechanism of ZAG is important not only in understanding how body fat mass is controlled, but also in uncovering the biochemical basis of its contribution to the pathology of type 2 diabetes.

The protein structure of ZAG exhibits a class I major histocompatibility complex (MHC) protein fold with two α -helices that define a groove [16]. However, ZAG is distinct from other MHC immune proteins in three aspects: (i) ZAG is soluble, rather than being anchored to plasma membranes; (ii) ZAG associates with prolactin-inducible protein rather than β_2 -microglobulin [17], and (iii) ZAG binds small hydrophobic ligands rather than antigenic peptides in its α -helical groove [18]. Unlike the classic MHC proteins, the binding groove in ZAG contains one charged residue Arg73, but is otherwise lined by hydrophobic residues [16]. In keeping with this observation, site-directed mutagenesis and fluorescence measurements revealed that ZAG binds polyunsaturated fatty acids with μ M affinity in its groove [19]. The actual ligand occupying the ZAG groove *in vivo* has yet to be discovered and will be crucial to understanding the molecular mechanism of ZAG. To initiate this analysis, we have shown that ZAG contains one tightly-bound zinc ion, predicted to bind close to its groove, plus approximately 15 weak zinc binding sites on the protein surface [20]. The weak zinc binding sites are deemed responsible for the precipitation of ZAG from plasma [2].

Here, we analyse the relationship of zinc binding to ZAG with its presumed lipid-binding function using a combination of biophysical approaches. Using analytical ultracentrifugation (AUC), small angle X-ray scattering (SAXS) and circular dichroism (CD) to monitor the oligomerisation and conformation of ZAG, we show that the weak zinc binding sites are specific only for zinc, and not for other bivalent metals, and zinc causes ZAG to self-associate to form oligomers. The use of SAXS and AUC molecular modelling showed that the oligomers form via a stacking mechanism which occludes the ZAG groove. The use of a fluorescent-labelled fatty acid permitted a recently-developed method termed fluorescent-detected AUC (AUC-FDS) to follow the binding of a fluorescent-labelled fatty acid C₁₆-BODIPY to ZAG, which further revealed that zinc also promotes oligomerisation of the C₁₆-BODIPY:ZAG complex. Fluorescence spectroscopy demonstrated that ZAG binds the fluorescent fatty acid C₁₆-BODIPY in a hydrophobic environment but that the binding of C₁₆-BODIPY to ZAG was abrogated with increasing zinc concentrations. In contrast the binding of the fluorescent dansylated C₁₀-fatty acid, DAUDA, to ZAG was not affected by additions of zinc. We show for the first time that the ZAG groove contains multiple fatty acid binding sites, and discuss the functional significance of this outcome.

EXPERIMENTAL

Purification of ZAG in the presence of divalent metals

Starting from a pET23a clone containing human ZAG, ZAG was purified from inclusion bodies using 6 M guanidine hydrochloride [20]. Denatured ZAG was gradually added to 1 L refolding buffer at 4°C. Vivaspin centrifugal concentrators (MWCO 10 kDa; Sartorius) were used to concentrate the refolded ZAG solution to 5 ml. ZAG was dialyzed overnight against 1 L of 10 mM Hepes, 137 mM NaCl, pH 7.4 (Hepes buffer) at 4°C with three buffer changes. ZAG was further purified using a GE Superdex 200 size-exclusion chromatography column equilibrated with Hepes buffer at a flow rate of 2 ml/min. Fractions corresponding to the ZAG elution peak were collected and its purity was confirmed by the observation of a single band on 15% SDS PAGE corresponding to the 32 kDa ZAG protein [20]. The concentration of ZAG was determined using a spectrophotometer (Perkin Elmer Lambda 35) with a theoretical molecular mass of 32,278 Da and extinction coefficient of $71,071 \text{ M}^{-1}\text{cm}^{-1}$ calculated from the amino acid content [21]. The protein was used immediately in experiments. Analytical size-exclusion chromatography was performed using a Superdex 75 gel filtration column equilibrated with Hepes buffer on its own or with 2 mM of a metal chloride, pH 7.4, at a flow rate of 0.5 ml/min. 100 μL of 6.2 μM ZAG was injected onto the column in the absence and presence of 2 mM metal chlorides. Individual samples were run in duplicate. Native PAGE was performed using 4-20% Mini-PROTEAN Precast Gels (Bio-Rad).

Dynamic light scattering (DLS)

Dynamic light scattering, experiments were made with a Zetasizer Nano range instrument (Malvern). Sterile filtered ZAG (21 μM) in Hepes buffer was titrated with increasing concentrations of zinc and barium chlorides, followed by the addition of excess EDTA. Samples were measured in triplicate using 10 mm path length cuvettes at 25°C and assuming a buffer viscosity of 1.0300 cp.

Circular dichroism (CD)

An Applied Photophysics Chirascan Plus™ spectrometer (Leatherhead, UK) was used to measure the UV absorbance and the 'near and far-UV' CD spectra of ZAG titrated with increasing concentrations of metal chlorides (barium, calcium, manganese, cobalt, nickel and zinc). The UV absorbance and 'near-UV' CD spectra of ZAG were measured using a 10 mm path length cuvette in a wavelength range between 230-400 nm. The 'far-UV' CD spectra of ZAG were measured using a 0.5 mm path length cuvette in a wavelength range between 190-260 nm. The CD instrument was flushed continuously with nitrogen gas and all spectra were recorded using a 1 nm spectral bandwidth, 1 nm step size and a 1.5 s instrument time-per-point. All measurements were made at 23°C using 6.2 μM ZAG and metal ion solutions in 10 mM Hepes, pH 7.4. A buffer baseline was subtracted from each sample spectrum prior to correction for the effects of dilution.

Analytical ultracentrifugation (AUC) and fluorescence detected AUC (AUC-FDS)

AUC experiments were performed using two XL-I Beckman-Coulter instruments equipped with An50Ti rotors, using velocity cells with two-sector aluminium centrepieces at rotor speeds of 50,000 rpm at 20°C. Sedimentation velocity experiments were performed with 6.2 μM ZAG in Hepes buffer which was titrated with zinc or barium chloride at concentrations of 0 mM, 0.5 mM, 1.0 mM and 2 mM metal, and with 7.5 mM EDTA. The buffer density for each sample was determined using an Anton Paar DMA 5000 density meter. SEDFIT software (version 14.6) was used to analyse the absorbance data recorded at 280 nm. The Lamm equation was directly fitted to every third boundary scan of a total of 150 scans in order to obtain the size distribution analysis $c(s)$ that provided the $s_{20,w}$ and mass values. The $c(s)$ analyses were based on a fixed resolution of 200, minimum and maximum sedimentation coefficients (S_{min} and S_{max}) of 0.5 S and 15 S respectively, a frictional ratio of 1.2, a meniscus of 6.2 cm, the bottom of the cell set at 7.2 cm, a confidence level (F -ratio) of 0.95, a partial specific volume of 0.730 ml/g, and buffer viscosity of 1.02369 cp (theoretical value calculated using SEDNTERP software [22]). The baseline, meniscus and bottom of the cell were floated for the fits.

Using the integration function in the $c(s)$ analysis, the amounts of ZAG monomer and oligomers were quantitated. A fluorescence detector retrofit system (AVIV Biomedical) on one AUC instrument allowed AUC-FDS measurements of the sedimentation of 6.2 μM C₁₆-BODIPY (4, 4-difluoro-5, 7-dimethyl-4-bora-3a, 4a-diaza-s-indacene-3-hexadecanoic acid; $\lambda_{Exc} = 488$ nm) in the presence of 6.2 μM ZAG and 0.5 mM, 1.0 mM or 2.0 mM zinc chloride to be made. A five-channel charcoal epon calibration centre piece was used where channel A contained 100 nM fluorescein isothiocyanate (Sigma Aldrich). Data were analysed using SEDFIT software as described above.

Small angle X-ray scattering

SAXS measurements on ZAG were carried out at the European Synchrotron Radiation Facility (Grenoble, France) on the BioSAXS BM29 beam line in 7/8 multibunch beam mode [23, 24]. The X-ray wavelength was 0.0992 nm and the sample-detector distance was 2.87 m. The absence of radiation damage to the sample was confirmed through on-line checks at low Q values, and potential damage eliminated through the continuous movement of the flow cell during beam exposure. ZAG was loaded at a concentration of 0.5 mg/ml (15.5 μM) in Hepes buffer. Zinc and barium chloride concentrations were added to the protein in Hepes buffer 24 h before loading onto the beam line. Data was acquired in time frames of 1 s for 10 frames per run. For analyses, the final curves were averaged following the subtraction of 10 raw buffer files from 10 samples files. In a given solute-solvent contrast, the radius of gyration R_G is a measure of structural elongation if the internal inhomogeneity of scattering densities within the protein has no effect, being defined as the root mean square of distances within the protein relative to its centre of scattering density. Guinier analyses at low Q (where $Q = 4\pi \sin \theta/\lambda$; 2θ is the scattering angle and λ is the wavelength) gives the R_G and the forward scattering at zero angle $I(0)$ [25]:

$$\ln I(Q) = \ln I(0) - \frac{R_G^2 Q^2}{3}$$

The Guinier analyses were performed in a Q range of 0.20-0.42 nm^{-1} using SCT software [26]. The distance distribution function $P(r)$ was generated using GNOM software [27] and gives alternative determinations of the R_G and $I(0)$ values.

The theoretical X-ray scattering curve was calculated from the ZAG crystal structure (PDB code 1T7Z) [18], following its conversion from atomic coordinates to a coarse-grained model and the addition of hydration spheres using SCT software [26]. Putative ZAG oligomers were generated using PyMOL software and the ZAG crystal structure for similar calculations [18]. For ultracentrifugation modelling, the atomic coordinate files for the ZAG monomer and oligomers were inputted into the HydroPRO shell modelling software to generate theoretical sedimentation coefficient $s_{20,w}^0$ values [28].

Fluorescence spectroscopy

Fluorescence measurements were recorded at 22°C with a Perkin Elmer LS50B Luminescence Spectrometer (Bucks, UK) using 2 ml samples in a quartz cuvette, path length = 1 cm. The three fluorescent fatty acid probes C₁₁-BODIPY (4,4-difluoro-5,7-dimethyl-4-bora-3a-4a-diaza-s-Indacene-3-undecanoic acid), C₁₆-BODIPY and DAUDA (11-((5-dimethylaminonaphthalene-1-sulphonyl)amino)undecanoic acid) were obtained from Thermo Fisher Scientific Life Technologies. C₁₁- and C₁₆-BODIPY were both stored as stock solutions of ~3 mg/ml in DMSO. DAUDA was stored as a stock solution of ~1.5 mg/ml in ethanol. All fluorescent fatty acids were stored in the dark at -20 °C and freshly diluted before experiments into methanol, phosphate buffered saline (PBS; 137 mM NaCl, 20 mM Na₂HPO₄, 2.7 mM KCl and 1.5 mM KH₂PO₄) or Hepes buffer. The accurate concentrations of C₁₁- and C₁₆-BODIPY and DAUDA were calculated using $\epsilon_{550} = 86,000 \text{ M}^{-1} \text{ cm}^{-1}$, $\epsilon_{550} = 93,000 \text{ M}^{-1} \text{ cm}^{-1}$ and $\epsilon_{340} = 4,400 \text{ M}^{-1} \text{ cm}^{-1}$ in methanol respectively, all values obtained from the manufacturers' data sheets.

The fluorescence emission intensities of C₁₁-BODIPY and C₁₆-BODIPY were examined in methanol and PBS and upon addition of ZAG, ($\lambda_{ex} = 488$ nm). 0.89 μ M DAUDA ($\lambda_{ex} = 345$ nm) and 0.85 μ M C₁₆-BODIPY ($\lambda_{ex} = 488$ nm) were individually titrated with sequential additions of ZAG. The titrations were repeated in buffer containing 0.5 mM, 1 mM, 1.5 mM and 2 mM ZnCl₂. The titration curves were fitted using standard nonlinear regression techniques to a single noncompetitive binding model to generate dissociation constant K_d values [20]. Control experiments of 0.89 μ M DAUDA and 0.85 μ M C₁₆-BODIPY fluorescence emission in buffer containing 0, 0.5, 1.0, 1.5 and 2 mM ZnCl₂ revealed that the fluorescence emission of both probes were quenched upon addition of zinc. The quenching effect was accordingly corrected for this by subtraction of the DAUDA / C₁₆-BODIPY spectrum from the fluorescence emission profiles generated upon additions of ZAG. Fluorescence spectra were also corrected for the effects of dilution and, where noted, solvent Raman scattering was corrected by subtracting the buffer-only spectrum.

RESULTS

Metal-induced association of ZAG

In order to investigate why ZAG was precipitated by zinc and not by other metals, the metal binding specificity of ZAG was first examined by SEC, native PAGE and DLS. A much-decreased intensity of absorbance at 280 nm and a significant change in the ZAG elution time range (from 23 to 25 min) were observed upon addition of zinc, but not for the other five divalent metals tested (Figure 1A). Upon addition of zinc, the ZAG elution peak did not return to baseline, implying that ZAG-zinc had aggregated in the column and was gradually released upon further elution. In agreement with our previous study that revealed weak zinc binding to the surface of ZAG [20], these changes were reversible upon addition of EDTA. ZAG migrated as a single band on non-reducing native PAGE in the presence of seven divalent metals and in EDTA (Figure 1B). DLS revealed monomer ZAG to have a mean hydrodynamic radius R_h of 3.22 nm (Figure 1C, 1D; Table 1). Addition of increasing concentrations of zinc chloride to the ZAG solution caused the R_h value of ZAG to increase. In the presence of 2 mM zinc chloride, two peaks were observed corresponding to mean R_h values of 8.38 nm and 33.17 nm. These changes were reversed upon addition of excess EDTA where the mean R_h value of ZAG reverted back to 4 nm. Control experiments with the buffer alone in the absence of ZAG confirmed these results were due to ZAG-zinc complex formation. In contrast, titrating ZAG with increasing concentrations of barium chloride did not increase the mean R_h value of ZAG above 4.63 nm (Figure 1C, 1D; Table 1). It was inferred that zinc-ZAG aggregates were detected by DLS that were too weakly associated to be resolved using size-exclusion chromatography and native PAGE. In agreement with this, we had previously measured a K_d of 100 μ M for the strongest of the weak zinc binding sites in ZAG [20].

To probe further the metal binding specificity of ZAG, UV spectroscopy measurements were made to follow turbidity changes in ZAG. In agreement with our DLS observations, addition of 1.8 mM zinc chloride to ZAG, but not the other divalent metal ions, significantly increased the apparent absorbance over the entire wavelength range of 240-400 nm (Figure 2A). The apparent absorbance increase was attributed to underlying turbidity contributions. The existence of turbidity (light scattering), totally responsible for the apparent absorbance above 310 nm, indicated that ZAG forms aggregates in the presence of Zn²⁺ ions. Co²⁺ and Ni²⁺ ions also caused slight increases in absorbance (turbidity) upon addition to ZAG, but these were negligible compared with Zn²⁺. Through monitoring turbidity changes at 340 nm, the titrations of ZAG with five divalent metal chlorides confirmed a zinc-specific effect with the zinc-induced precipitation or aggregation displaying a sigmoidal curve (Figure 2B). Even though calcium and barium can form divalent complexes with negatively charged residues on proteins, here neither Ca²⁺ nor Ba²⁺ produced turbidity. Ca²⁺ and Ba²⁺ ions are larger and less charge-dense than Zn²⁺ ions and obviously not conducive to the formation of ZAG oligomers.

These metal-specific changes were further confirmed using CD to follow conformational changes in ZAG. The 'near-UV' CD spectrum of ZAG was significantly altered upon addition of zinc chloride, while only minor alterations in the spectrum were observed upon addition of cobalt or nickel chloride (Figure 2C). This result suggests that metal-induced changes occurred in the tertiary structure of ZAG that followed the order zinc > nickel \cong cobalt. Our observations were in line with the Irving-Williams series of transition metals which stated that the stability of metal : protein complexes follows the order Mn < Fe < Co < Ni < Cu > Zn [29]. The 'far-UV' CD spectrum of ZAG showed no significant changes in the broad negative peak at 218 nm upon addition of 1.8 mM of barium, calcium, manganese, cobalt and nickel chlorides, also suggesting no significant changes in the secondary structure of ZAG (Figure 2D). Addition of 1.8 mM zinc chloride decreased the intensity of the broad negative peak observed at 218 nm, showing a significant change in the 'far-UV' CD spectrum compared with that of ZAG alone, suggesting zinc-induced conformational changes had occurred in the secondary structure of ZAG.

Oligomeric structure of zinc-induced aggregates of ZAG

To identify the nature of the zinc-specific ZAG aggregates, AUC measurements were performed with ZAG in the presence of zinc chloride, with barium chloride used as a control. Samples were subjected to a high centrifugal force, and an absorbance optical system was used to observe the sedimentation of ZAG in real time. The sedimentation boundaries (Figures 3A-C) were well fitted to size distribution analyses (Experimental). In comparison with ZAG alone, more rapid sedimentation boundaries were observed upon addition of 2 mM ZnCl₂ (Figures 3A, 3B). In contrast, the addition of 2 mM BaCl₂, caused no significant changes in sedimentation compared to ZAG alone (Figure 3C). Size distribution *c(s)* analyses for the five zinc and barium concentrations revealed the presence of a ZAG monomer peak at a mean *s*_{20,w} value of 2.83 ± 0.02 S (Figure 3D and 3E). Mass distribution *c(M)* plots showed that this ZAG monomer peak corresponded to a mean molecular mass of 32 ± 0.5 kDa, which agreed well with the sequence-determined mass of 32 kDa. The intensities of the ZAG monomer peak were significantly reduced with additions of zinc, but not with barium. The *c(s)* analyses further showed that increasing the concentrations of zinc chloride to 1 mM and 2 mM gave rise to two additional peaks at *S* values of 4.07 S and 5.2 S that correspond to molecular masses of 68 kDa and 103 kDa, respectively (Figure 3D). These peaks correspond well to ZAG dimer and trimer formation. The broad nature of these dimer and trimer peaks indicated that these peaks may also correspond to low proportions of other ZAG oligomers of increased sizes in equilibrium with the monomer, dimer and trimer peaks. In contrast to zinc, an almost insignificant oligomer peak was visible for barium. The integrations of Figure 3F showed that the oligomers increased with decrease in ZAG monomer in the case of zinc, but not with barium. These protein-zinc oligomers have been seen previously; the human complement regulator factor H, complement protein C3 [30], and adiponectin also form oligomers in the presence of zinc [31], while zinc induces dimerization of the class II MHC molecule HLA-DR1 in a complex with a hemagglutinin peptide [32].

To determine whether similar ZAG-zinc oligomers were formed in the presence of fatty acids, AUC-FDS measurements were performed to track the movement of the fluorescent fatty acid C₁₆-BODIPY. In the presence of 0.5 mM ZnCl₂ and ZAG, a fluorescent sedimentation boundary was observed for C₁₆ BODIPY (Figure 4A). This corresponded to a ZAG monomer peak of mean *s*_{20,w} value 2.72 S in the *c(S)* analysis, indicating that C₁₆-BODIPY was bound to sedimenting ZAG in the presence of 0.5 mM ZnCl₂ (Figure 4E). No fluorescent sedimentation was observed for C₁₆-BODIPY on its own. The addition of 2 mM ZnCl₂ revealed more rapidly moving fluorescent sedimentation boundaries (Figure 4C). Indeed the *c(s)* analyses showed that increasing the concentrations of zinc chloride to 1 mM and 2 mM gave rise to ZAG-C₁₆-BODIPY *s*_{20,w} values of 4.14 S and 4.93 S that corresponded to molecular masses of 53 kDa and 70.2 kDa, respectively (Figure 4D). These two fluorescent peaks corresponded approximately to ZAG-C₁₆-BODIPY dimer and trimer formation. Following completion of this AUC-FDS experiment, the samples were re-suspended for conventional absorbance AUC that followed only

the sedimentating protein. This control revealed similar results with regards to the sedimentation boundaries (Figures 4B and 4D) to those in Figure 3B. The absorbance $c(s)$ analyses showed a monomer peak and a partly-formed dimer peak upon addition of 2 mM ZnCl_2 (Figure 4F), although no trimer peak was now observable, attributable to the different type of experiment in use.

To observe further the overall structure of ZAG, SAXS measurements were performed with ZAG in the presence and absence of Zn^{2+} and Ba^{2+} . SAXS data collection is sensitive to aggregate formation. For the ZAG-zinc interaction in one session, experiments were performed at a pH of 6.9 in the same Hepes buffer, and these showed that the R_G values of ZAG increased from 2.48 nm to 2.71 nm in linear Guinier plots on going from 0 mM zinc to 2 mM zinc (data not shown). This R_G increase indicated oligomer formation, however SAXS was not able to resolve more detail than this. These R_G increases did not occur in the presence of increasing barium chloride concentrations. For the ZAG-barium titration series in a second session, the Guinier fits also gave high quality linear fits with R_G values of between 2.41 ± 0.01 nm and 2.48 ± 0.01 nm in satisfactory $Q \cdot R_G$ ranges (Figure 5A). These were in good agreement with the R_G value of 2.58 ± 0.01 nm for ZAG alone. The distance distribution function $P(r)$ was calculated from the full scattering curve $I(Q)$ to produce a histogram of the distances between all the pairs of atoms within ZAG. From the $P(r)$ curve, the R_G value was determined to be 2.32 ± 0.27 nm with a maximum dimension L of 8 nm (Figure 5B). Again, neither the R_G nor the L values changed significantly upon addition of increasing BaCl_2 concentrations. Inspection of the unhydrated ZAG crystal structure showed that its maximum dimension is 7.4 nm, which is 0.5 nm less than the L value of ZAG from the $P(r)$ curves. This difference is attributable to the thickness of the water hydration shell surrounding the ZAG protein surface [33]. In order to confirm that the ZAG crystal structure corresponds to its structure in solution, the excellent scattering curve fit of the experimental data with the theoretical curve calculated from the hydrated ZAG crystal structure showed that ZAG is well represented in solution by its atomistic crystal structure (Figure 5C).

Fatty acid binding to ZAG in the absence and presence of zinc

The dansylated C_{11} fatty acid probe, DAUDA, has previously been shown to bind between the $\alpha 1$ and $\alpha 2$ domain helices of ZAG by site-directed mutagenesis studies [19]. For AUC-FDS studies, the DAUDA excitation and emission parameters do not match those of the fluorescence detector, so could not be used. Instead, the boron dipyrromethene fatty acid probe C_{16} -BODIPY was used, given that its excitation and emission parameters match the AUC-FDS detector. To confirm that C_{16} -BODIPY bound as expected to ZAG, the fluorescence profiles of C_{11} -BODIPY and C_{16} -BODIPY were recorded to reveal low fluorescent emissions at a wavelength maximum of 511 nm in PBS (Figure 6A and 6B). In methanol, these fluorescence emission intensities were dramatically increased (Figure 6A and 6B). Addition of ZAG to C_{16} -BODIPY in PBS produced a large increase in fluorescence emission intensity and a red shift in the wavelength maximum of emission (from 512 nm to 518 nm; Figure 6C) suggesting that C_{16} -BODIPY has bound to ZAG in a more hydrophobic environment, which was presumed to be the ZAG groove. A similar shift (from 514 nm to 518 nm) and increase in intensity were reported for the binding of intracellular liver and intestinal type fatty acid binding proteins to C_{16} -BODIPY [34]. On the contrary, the fluorescence emission intensity of C_{11} -BODIPY did not change significantly upon the addition of ZAG (Figure 6D), indicating that C_{11} -BODIPY did not bind to ZAG. Importantly this experiment revealed that the boron dipyrromethene moiety of BODIPY did not associate with ZAG, and that the C_{16} fatty acid was preferred over C_{11} -BODIPY in binding to ZAG. Interestingly, ZAG binds DAUDA but not C_{11} -BODIPY, both of which contain undecanoic acid as the fatty acid chain. The DAUDA binding site in ZAG is not attributable to the dansyl fluorophore given that this alone does not bind to ZAG [35]. Because no long chain derivatives of DAUDA currently exist, we were unable to compare long and short chain fatty acid binding using dansylated fatty acids. We presume that the larger size of the BODIPY moiety compared to the dansyl moiety, prevents the binding of its undecanoic fatty acid to its site in ZAG.

To determine whether the zinc-ZAG oligomers showed altered functional properties in binding to fatty acids, ZAG titrations were performed using C₁₆-BODIPY and DAUDA in the absence and presence of Zn²⁺. Incremental additions of ZAG protein to C₁₆-BODIPY caused increased intensities and a red shift in the C₁₆-BODIPY fluorescence emission, and these reached saturation upon the addition of approximately 2 μM ZAG (Figure 7A). A standard hyperbolic/non-cooperative binding model based on a 1:1 stoichiometry gave a ZAG: C₁₆-BODIPY dissociation constant K_d of 0.06 ± 0.01 μM (Table 2; Figure 7A). The C₁₆-BODIPY fluorescence emission was quenched upon addition of Zn²⁺ (Figure 7B). Quenching was presumed to occur via photo-induced electron transfer though the association of zinc with the deprotonated carboxylic acid of C₁₆-BODIPY (pK_a ~ 5) and the lone pair of the nitrogen atom disrupting the molecular C=C framework within the BODIPY moiety. The presence of increasing Zn²⁺ concentrations reduced the ability of ZAG to bind C₁₆-BODIPY; the K_d values increased to between 8.7 – 22.8 μM indicative of weaker binding of C₁₆-BODIPY to ZAG-zinc (Table 2, Figure 7C). In marked contrast to C₁₆-BODIPY, DAUDA binding to ZAG was not significantly affected by the presence of increasing Zn²⁺ concentrations. Upon addition of ZAG, the DAUDA emission underwent a blue shift from 543 nm to 519 nm with an increase in emission intensity that reached saturation upon addition of approximately 0.2 μM ZAG (Figure 7D). Fitting of this data to a standard hyperbolic/non-cooperative binding model based on a 1:1 stoichiometry gave a ZAG: DAUDA K_d value of 0.11 ± 0.01 μM (Table 2). We previously reported quenching of DAUDA fluorescence upon addition of Zn²⁺ [20] although the effect is markedly smaller in comparison to the quenching of C₁₆-BODIPY by Zn²⁺ (Figure 7E). When the ZAG-DAUDA titration was repeated in the presence of 0.5 mM, 1 mM and 1.5 mM ZnCl₂ (Figure 7F), similar titration curves were observed with unchanged K_d values of 0.05 – 0.07 μM (Table 2). In 2 mM ZnCl₂, a larger increase in the fluorescence emission intensity was observed together with a K_d value of 0.17 μM⁻¹. Overall, it was concluded that, unlike C₁₆-BODIPY, DAUDA is able to bind to ZAG-zinc oligomers.

Modelling of ZAG-zinc oligomer formation

To clarify a molecular mechanism for the zinc-induced oligomerisation of ZAG, structures for the ZAG oligomers were modelled, starting from the knowledge that the X-ray scattering curve of ZAG fitted its crystal structure (Figure 5C). By trial and error, an arrangement of ZAG oligomers that generated close agreement between the experimental and theoretical $s_{20,w}$ values was found to involve the compact stacking of ZAG monomers on top of each other in the same orientation (Figure 8A). The experimental $s_{20,w}$ values were 2.70 S, 4.07 S and 5.20 S for the monomer, dimer and trimer; the modelled values were 2.57 S, 4.08 S and 5.30 S respectively. This good agreement is well within the error of ±0.21 S for these comparisons [36]. Previously, we showed that the surface of ZAG contains approximately 15 weak zinc binding sites [20]. The surface of ZAG is rich in negatively-charged acidic Asp and Glu residues (Figure 8B). Zn²⁺ adopts tetrahedral co-ordination with proteins, typically involving Asp, Glu, His and Cys residues [37], of which there are 18 Asp, 21 Glu, 7 His and 4 Cys residues in ZAG. While the four Cys residues are involved in intramolecular disulphide bridge formation, all the Asp and Glu residues are located on the ZAG surface. Presumably the stacking of ZAG into dimers and trimers is stabilised by the formation of weak zinc binding sites at an extensive interface formed between compactly-associated ZAG monomers in which zinc crosslinks these surface Asp and Glu residues. Because oligomer formation can be extended indefinitely in such an arrangement, this stacking model provides an explanation for why ZAG is precipitated by Zn²⁺ at high Zn²⁺ concentrations.

DISCUSSION

Our investigations revealed new insights into the ZAG-zinc and ZAG-fatty acid complexes and their functional significance. Thus we have developed a molecular model for the stacking of ZAG-zinc oligomers from the modelling of the SAXS and AUC data, and this is able to explain how ZAG is precipitated by excess zinc. Such a model suggests that, as the Zn²⁺ concentration increases, the ZAG

lipid-binding groove will be shielded and inhibit the ability of ZAG to bind fatty acids. This deduction accounts for our observation of reduced C₁₆-BODIPY binding to ZAG in the presence of increasing Zn²⁺ concentrations (Figure 7A). Notably the same effects were not observed for DAUDA (Figure 7B). This difference can be explained by the existence of at least two distinct lipid binding sites in the ZAG groove, one for each of DAUDA (unaffected by ZAG-zinc stacking) and C₁₆-BODIPY (inhibited by ZAG-zinc stacking). More support for the concept of two different binding sites is provided as follows:

(i) The interaction of DAUDA with ZAG is well characterized. Arachidonic and docosahexaenoic acids are able to displace DAUDA from the ZAG groove [35, 18]. The ZAG groove contains five tryptophan residues whose fluorescence is quenched and blue shifted upon addition of arachidonic and docosahexaenoic acids. However no binding data for these fatty acids had been reported in these studies, and we have not investigated this here. In addition, site-directed mutagenesis has shown that mutation of the hydrophobic groove residues Y14, F101, I76 and Y154 and the positively charged groove residue R73 abrogates DAUDA binding to ZAG by complete or partial closure of the groove [19]. Arginine and lysine residues also act as tethers of fatty acids in human serum albumin and β -lactoglobulin [38, 39]. The ZAG groove contains lysine and tyrosine residues which have not been examined so far by site-directed mutagenesis.

(ii) C₁₆-BODIPY binds to ZAG with a K_d = 0.06 μ M, which is slightly stronger than DAUDA (K_d = 0.11 μ M). DAUDA binds to human plasma apolipoprotein D with a similar K_d value of 0.54 μ M [40] and likewise arachidonic acid with a K_d = 1 μ M [41]. These K_d values make it unlikely therefore that the C₁₆-BODIPY binding to ZAG is a non-specific surface interaction. This conclusion is reinforced by the spectroscopic changes seen by fluorescence (Figures 6A and 6C).

(iii) Two distinct lipid binding sites were observed in the crystal structure of CD1c, another member of the MHC class 1-like immune protein family that present bacterial lipid based antigens to T-cells [42]. The crystal structures of five human CD1a-CD1e molecules show two main hydrophobic domains (called A' and F') (Figure 8C) which vary in size according to the length of the hydrophobic chains that they bind [43]. Our results with ZAG show a similar observation with this different member of the MHC class 1-like immune protein family, albeit using fluorescently labelled fatty acids.

In humans, ZAG expression is reduced in plasma and adipocytes of patients with type 2 diabetes, and is associated with insulin resistance [7, 8, 44]. Levels of ZAG are increased in urine from patients with type 1 and type 2 diabetes compared with controls [9, 10]. Similarly, pancreatic zinc is approximately 50% less in cadavers of diabetic patients compared with non-diabetic cadavers [45] and increased urinary zinc levels are observed in diabetes [46, 47]. The total plasma zinc level is about 14.7 μ M [48] of which the overwhelming majority is bound to human serum albumin as the main zinc buffer in plasma [49]. Bioavailable zinc in blood plasma is therefore very low at around 20-210 pM [50], this being insufficient to induce ZAG precipitation. In contrast to this, the total zinc concentration of the mammalian pancreas is significantly higher than other cell types [51] with zinc concentrations reaching 10–20 mM in the interior of the dense-core of beta cell granules [51]. Insulin is stored in the pancreatic beta cell granules in crystalline arrays of hexamers containing two zinc ions per hexameric unit [52]. Upon secretion from the pancreas into the blood stream the complex dissociates forming monomeric insulin. Although ZAG is not expressed in the pancreatic beta-cell granules, ZAG has been reported in acinar and peripheral cells of healthy human pancreatic islets [3]. It appears likely that ZAG-zinc oligomers are stored in the pancreatic beta cells in a manner similar to insulin. Islet amyloid polypeptide or amylin, a neuropancreatic hormone involved in the regulation of a range of metabolic parameters forms toxic pancreatic islet amyloid in type 2 diabetes [53]. Amylin contains two zinc binding sites; one binds zinc tightly with a K_d value of 1 μ M and the other binds zinc loosely with a K_d value of about 1 mM. Both zinc binding sites prevent amylin forming amyloid fibrils [53]. We previously measured a K_d = 100 μ M for the strongest of the weak zinc binding sites in ZAG. We speculate therefore that ZAG-zinc oligomers participate in the formation of pancreatic amylin plaques in type 2 diabetes by sequestering high concentrations of zinc.

In conclusion, divalent metal binding by ZAG is zinc-specific. Zinc induces the oligomerization of ZAG in the absence and presence of fatty acids. The fluorescently-labelled fatty acid C₁₆-BODIPY binds to ZAG, while C₁₁-BODIPY does not. The binding of C₁₆-BODIPY to ZAG is reduced in the presence of increasing zinc concentrations, but DAUDA binding is almost unaffected. These data support a progressive stacking of monomeric ZAG in the presence of Zn²⁺ whereby the ZAG groove becomes partially occluded to suggest the presence of two distinct lipid binding sites in ZAG. Our observation may be relevant to storage of ZAG in the pancreas. It will be interesting to discover if toxic pancreatic amyloid in type 2 diabetes contains ZAG as well as amylin.

ACKNOWLEDGEMENTS (including declarations of interest if any)

We thank Dr Alexander Alexandrovich and Dr A. James Mason for the use of gel filtration columns, Dr Lea Ann Dailey for the use of a DLS machine, Ms Gar Kay-Hui for help with SAXS analyses and Dr David W. Wright for computational support. L.C.McD holds a purchasing and licencing agreement with the Biotech Company AdipoGen.

AUTHOR CONTRIBUTION

H.Z., L.M, A.M.L., L.B., D.H., T.T.T.B., A.F.D., J.G., S.J.P. and L.C.McD. designed and performed research, analyzed data and wrote the manuscript.

FUNDING

Support for this work was also provided in part by the CCP-SAS project, a joint EPSRC (EP/K039121/1) and NSF (CHE-1265821) grant.

REFERENCES

- 1 World Health Organisation (2015) Fact sheet No. 312, Diabetes.
- 2 Burgi, W. and Schmid, K. (1961) Preparation and properties of Zn-alpha 2-glycoprotein of normal human plasma. *J. Biol. Chem.* **236**, 1066-1074
- 3 Kong, B., Michalski, C. W., Hong, X., Valkovskaya, N., Rieder, S., Abiatari, I., Streit, S., Erkan, M., Esposito, I., Friess, H. and Kleeff, J. (2010) AZGP1 is a tumor suppressor in pancreatic cancer inducing mesenchymal-to-epithelial transdifferentiation by inhibiting TGF-beta-mediated ERK signaling. *Oncogene.* **29**, 5146-5158
- 4 Bao, Y., Bing, C., Hunter, L., Jenkins, J. R., Wabitsch, M. and Trayhurn, P. (2005) Zinc-alpha2-glycoprotein, a lipid mobilizing factor, is expressed and secreted by human (SGBS) adipocytes. *FEBS Lett.* **579**, 41-47
- 5 Mracek, T., Stephens, N. A., Gao, D., Bao, Y., Ross, J. A., Ryden, M., Arner, P., Trayhurn, P., Fearon, K. C. and Bing, C. (2011) Enhanced ZAG production by subcutaneous adipose tissue is linked to weight loss in gastrointestinal cancer patients. *Br. J. Cancer.* **104**, 441-447
- 6 Selva, D. M., Lecube, A., Hernandez, C., Baena, J. A., Fort, J. M. and Simo, R. (2009) Lower zinc-alpha2-glycoprotein production by adipose tissue and liver in obese patients unrelated to insulin resistance. *J. Clin. Endocrinol. Metab.* **94**, 4499-4507
- 7 Balaz, M., Vician, M., Janakova, Z., Kurdiová, T., Surova, M., Imrich, R., Majercikova, Z., Penesova, A., Vlcek, M., Kiss, A., Belan, V., Klimes, I., Olejnik, J., Gasperikova, D., Wolfrum, C., Ukropcova, B. and Ukropec, J. (2014) Subcutaneous adipose tissue zinc-alpha2-glycoprotein is associated with adipose tissue and whole-body insulin sensitivity. *Obesity (Silver Spring).* **22**, 1821-1829

- 8 Yang, M., Liu, R., Li, S., Luo, Y., Zhang, Y., Zhang, L., Liu, D., Wang, Y., Xiong, Z., Boden, G., Chen, S., Li, L. and Yang, G. (2013) Zinc-alpha2-glycoprotein is associated with insulin resistance in humans and is regulated by hyperglycemia, hyperinsulinemia, or liraglutide administration: cross-sectional and interventional studies in normal subjects, insulin-resistant subjects, and subjects with newly diagnosed diabetes. *Diabetes Care*. **36**, 1074-1082
- 9 Riaz, S., Alam, S. S., Srail, S. K., Skinner, V., Riaz, A. and Akhtar, M. W. (2010) Proteomic identification of human urinary biomarkers in diabetes mellitus type 2. *Diabetes Technol. Ther.* **12**, 979-988
- 10 Soggiu, A., Piras, C., Bonizzi, L., Hussein, H. A., Pisanu, S. and Roncada, P. (2012) A discovery-phase urine proteomics investigation in type 1 diabetes. *Acta Diabetol.* **49**, 453-464
- 11 Olofsson, L. E., Olsson, B., Lystig, T., Jacobson, P., Jernås, M., Sjöholm, K., Gummesson, A., Sjöström, L., Eriksson, P., Hamsten, A., Hale, L. P., Thelle, D. S., Carlsson, B. and Carlsson, L. M. S. (2010) Preliminary report: Zn-alpha2-glycoprotein genotype and serum levels are associated with serum lipids. *Metabolism*. **59**, 1316-1318
- 12 Zhu, H. J., Dong, C. X., Pan, H., Ping, X. C., Li, N. S., Dai, Y. F., Wang, L. J., Yang, H. B., Zhao, W. G. and Gong, F. Y. (2012) rs4215 SNP in zinc-alpha2-glycoprotein gene is associated with obesity in Chinese north Han population. *Gene*. **500**, 211-215
- 13 Ryden, M., Agustsson, T., Andersson, J., Bolinder, J., Toft, E. and Arner, P. (2012) Adipose zinc-alpha2-glycoprotein is a catabolic marker in cancer and noncancerous states. *J. Intern. Med.* **271**, 414-420
- 14 Russell, S. T. and Tisdale, M. J. (2010) Antidiabetic properties of zinc-alpha2-glycoprotein in ob/ob mice. *Endocrinology*. **151**, 948-957
- 15 Eckardt, K., Schober, A., Platzbecker, B., Mracek, T., Bing, C., Trayhurn, P. and Eckel, J. (2011) The adipokine zinc-alpha2-glycoprotein activates AMP kinase in human primary skeletal muscle cells. *Arch. Physiol. Biochem.* **117**, 88-93
- 16 Sanchez, L. M., Chirino, A. J. and Bjorkman, P. (1999) Crystal structure of human ZAG, a fat-depleting factor related to MHC molecules. *Science*. **283**, 1914-1919
- 17 Hassan, M. I., Bilgrami, S., Kumar, V., Singh, N., Yadav, S., Kaur, P. and Singh, T. P. (2008) Crystal structure of the novel complex formed between zinc alpha2-glycoprotein (ZAG) and prolactin-inducible protein (PIP) from human seminal plasma. *J. Mol. Biol.* **384**, 663-672
- 18 Delker, S. L., West, A. P., Jr., McDermott, L., Kennedy, M. W. and Bjorkman, P. J. (2004) Crystallographic studies of ligand binding by Zn-alpha2-glycoprotein. *J. Struct. Biol.* **148**, 205-213
- 19 McDermott, L. C., Freel, J. A., West, A. P., Bjorkman, P. J. and Kennedy, M. W. (2006) Zn-alpha2-glycoprotein, an MHC class I-related glycoprotein regulator of adipose tissues: modification or abrogation of ligand binding by site-directed mutagenesis. *Biochemistry*. **45**, 2035-2041
- 20 Kumar, A. A., Hati, D., Thaker, T. M., Miah, L., Cunningham, P., Domene, C., Bui, T. T., Drake, A. F. and McDermott, L. C. (2013) Strong and weak zinc binding sites in human zinc-alpha2-glycoprotein. *FEBS Lett.* **587**, 3949-3954
- 21 Gill, S. C., von Hippel, P. H. (1989) Calculation of protein extinction coefficients from amino acid sequence data. *Anal. Biochem.* **182**(2), 319-26.

- 22 Laue T. M., Shah B. D., Ridgeway T. M., Pelletier S. L. (1992) in *Analytical Ultracentrifugation in Biochemistry and Polymer Science* (Harding S. E., Rowe A. J., Horton J. C., eds) pp. 90–125, Royal Society of Chemistry, Cambridge, UK
- 23 Pernot, P., Round, A., Barrett, R., De Maria Antolinos, A., Gobbo, A., Gordon, E., Huet, J., Kieffer, J., Lentini, M., Mattenet, M., Morawe, C., Mueller-Dieckmann, C., Ohlsson, S., Schmid, W., Surr, J., Theveneau, P., Zerrad, L. and McSweeney, S. (2013) Upgraded ESRF BM29 beamline for SAXS on macromolecules in solution. *J Synchrotron Radiat.* **20**, 660-664
- 24 Round, A., Felisaz, F., Fodinger, L., Gobbo, A., Huet, J., Villard, C., Blanchet, C. E., Pernot, P., McSweeney, S., Roessle, M., Svergun, D. I. and Cipriani, F. (2015) BioSAXS Sample Changer: a robotic sample changer for rapid and reliable high-throughput X-ray solution scattering experiments. *Acta Crystallogr. D Biol. Crystallog.* **71**, 67-75
- 25 Glatter O., Kratky O.(1982) *Small Angle X-ray Scattering*, pp. 17–51, Academic Press, Inc., New York
- 26 Wright, D. W. and Perkins, S. J. (2015) SCT: a suite of programs for comparing atomistic models with small-angle scattering data. *J. App. Crystallog.* **48**, 953-961
- 27 Semenyuk, A. V. and Svergun, D. I. (1991) GNOM - a program package for small-angle scattering data processing. *J. App. Crystallog.* **24**, 537-540
- 28 Garcia de la Torre, J., Navarro, S., Lopez Martinez, M. C., Diaz, F. G. and Lopez Cascales, J. J. (1994) HYDRO: a computer program for the prediction of hydrodynamic properties of macromolecules. *Biophys. J.* **67**, 530-531
- 29 Irving, H. and Williams, R. J. P. (1953) 637. The stability of transition-metal complexes. *J. Chem. Soc. (Resumed)*, 3192-3210
- 30 Nan, R., Tetchner, S., Rodriguez, E., Pao, P. J., Gor, J., Lengyel, I. and Perkins, S. J. (2013) Zinc-induced self-association of complement C3b and Factor H: implications for inflammation and age-related macular degeneration. *J. Biol. Chem.* **288**, 19197-19210
- 31 Briggs, D. B., Giron, R. M., Schnittker, K., Hart, M. V., Park, C. K., Hausrath, A. C. and Tsao, T. S. (2012) Zinc enhances adiponectin oligomerization to octadecamers but decreases the rate of disulfide bond formation. *Biometals.* **25**, 469-486
- 32 Li, H., Zhao, Y., Guo, Y., Li, Z., Eisele, L. and Mourad, W. (2007) Zinc induces dimerization of the class II major histocompatibility complex molecule that leads to cooperative binding to a superantigen. *J. Biol. Chem.* **282**, 5991-6000
- 33 Perkins, S. J. (2001) X-ray and neutron scattering analyses of hydration shells: a molecular interpretation based on sequence predictions and modelling fits. *Biophys. Chem.* **93**, 129-139
- 34 Thumser, A. E. and Storch, J. (2007) Characterization of a BODIPY-labeled fluorescent fatty acid analogue. Binding to fatty acid-binding proteins, intracellular localization, and metabolism. *Mol. Cell. Biochem.* **299**, 67-73
- 35 Kennedy, M. W., Heikema, A. P., Cooper, A., Bjorkman, P. J. and Sanchez, L. M. (2001) Hydrophobic ligand binding by Zn-alpha 2-glycoprotein, a soluble fat-depleting factor related to major histocompatibility complex proteins. *J. Biol. Chem.* **276**, 35008-35013

- 36 Perkins, S. J., Okemefuna, A. I., Nan, R., Li, K. and Bonner, A. (2009) Constrained solution scattering modelling of human antibodies and complement proteins reveals novel biological insights. *J. R. Soc. Interface.* **6** Suppl 5, S676-S696.
- 37 Auld, D. (2001) Zinc coordination sphere in biochemical zinc sites. *Biometals.* **14**, 271-313
- 38 Petitpas, I., Grune, T., Bhattacharya, A. A., and Curry, S. (2001) Crystal structures of human serum albumin complexed with monounsaturated and polyunsaturated fatty acids, *J. Mol. Biol.* **314**, 955 - 960.
- 39 Wu, S.-Y., Perez, M. D., Puyol, P., and Sawyer, L. (1999) β -Lactoglobulin binds palmitate within its central cavity, *J. Biol. Chem.* **274**, 170-174.
- 40 Breustedt, D. A., Schönfeld, D. L., and Skerra, A. (2006) Comparative ligand-binding analysis of ten human lipocalins, *Biochim. Biophys. Acta* **1764**(2), 161–173.
- 41 Vogt, M. and Skerra, A. (2001) Bacterially produced apolipoprotein D binds progesterone and arachidonic acid, but not bilirubin or E-3M2H, *J. Mol. Recognit.* **14**(1), 79-86.
- 42 Brigl, M. and Brenner, M. B. (2004) CD1: antigen presentation and T cell function. *Ann. Rev. Immunol.* **22**, 817-890
- 43 Scharf, L., Li, N. S., Hawk, A. J., Garzon, D., Zhang, T., Fox, L. M., Kazen, A. R., Shah, S., Haddadian, E. J., Gumperz, J. E., Saghatelian, A., Faraldo-Gomez, J. D., Meredith, S. C., Piccirilli, J. A. and Adams, E. J. (2010) The 2.5 Å structure of CD1c in complex with a mycobacterial lipid reveals an open groove ideally suited for diverse antigen presentation. *Immunity.* **33**, 853-862
- 44 Garrido-Sanchez, L., Garcia-Fuentes, E., Fernandez-Garcia, D., Escote, X., Alcaide, J., Perez-Martinez, P., Vendrell, J. and Tinahones, F. J. (2012) Zinc-alpha 2-glycoprotein gene expression in adipose tissue is related with insulin resistance and lipolytic genes in morbidly obese patients. *PLoS One.* **7**, e33264
- 45 Scott, D. A. and Fisher, A. M. (1938) THE INSULIN AND THE ZINC CONTENT OF NORMAL AND DIABETIC PANCREAS. *J. Clin. Invest.* **17**, 725-728
- 46 Kinlaw, W. B., Levine, A. S., Morley, J. E., Silvis, S. E. and McClain, C. J. (1983) Abnormal zinc metabolism in type II diabetes mellitus. *Am. J. Med.* **75**, 273-277
- 47 Lau, A. L. and Failla, M. L. (1984) Urinary excretion of zinc, copper and iron in the streptozotocin-diabetic rat. *J. Nutr.* **114**, 224-233
- 48 Age-Related Eye Disease Study Research, G. (2001) A randomized, placebo-controlled, clinical trial of high-dose supplementation with vitamins c and e, beta carotene, and zinc for age-related macular degeneration and vision loss: Areds report no. 8. *Archives of Ophthalmology.* **119**, 1417-1436
- 49 Foote, J. W. and Delves, H. T. (1984) Albumin bound and alpha 2-macroglobulin bound zinc concentrations in the sera of healthy adults. *J. Clin. Pathol.* **37**, 1050-1054
- 50 Colvin, R. A., Holmes, W. R., Fontaine, C. P. and Maret, W. (2010) Cytosolic zinc buffering and muffling: their role in intracellular zinc homeostasis. *Metallomics.* **2**, 306-317
- 51 Li, Y. V. (2014) Zinc and insulin in pancreatic beta-cells. *Endocrine.* **45**, 178-189

52 Gavrilova, J., Tougu, V. and Palumaa, P. (2014) Affinity of zinc and copper ions for insulin monomers. *Metallomics*. **6**, 1296-1300

53 Brender, J. R., Krishnamoorthy, J., Messina, G. M. L., Deb, A., Vivekanandan, S., La Rosa, C., Penner-Hahn, J. E. and Ramamoorthy, A. (2013) Zinc stabilization of prefibrillar oligomers of human islet amyloid polypeptide. *Chem. Comm.* **49**, 3339-3341

Table 1. Mean hydrodynamic radius (R_h) of ZAG in Hepes buffer. Samples were titrated with zinc chloride or barium chloride followed by excess EDTA. Samples were examined in triplicate and the mean R_h value was reported with its standard error (SE).

21 μM ZAG	$R_h \pm SE$ (nm)	21 μM ZAG	$R_h \pm SE$ (nm)
+ 0.0 mM ZnCl ₂	3.22 \pm 0.18	+ 0.0 mM BaCl ₂	3.22 \pm 0.18
+ 0.5 mM ZnCl ₂	6.21 \pm 0.30	+ 0.5mM BaCl ₂	4.00 \pm 0.19
+ 1.0 mM ZnCl ₂	7.19 \pm 0.34	+ 1.0mM BaCl ₂	4.44 \pm 0.41
+ 1.5 mM ZnCl ₂	8.05 \pm 1.07	+ 1.5mM BaCl ₂	4.63 \pm 0.22
+ 2.0 mM ZnCl ₂	8.38 \pm 1.48	+ 2.0mM BaCl ₂	4.23 \pm 0.36
	33.17 \pm 9.70		
+ 2.0mM ZnCl ₂ + 7.5mM EDTA	4.00 \pm 0.19	+ 2.0mM BaCl ₂ + 7.5mM EDTA	4.41 \pm 0.22

Table 2. Dissociation constants K_d for ZAG binding to DAUDA and C₁₆-BODIPY in the presence and absence of ZnCl₂. The K_d values were generated from a non-competitive single binding site model.

[Zinc] (mM)	K_d (μM)	
	DAUDA	C₁₆-BODIPY
0.0	0.11 \pm 0.01	0.06 \pm 0.01
0.5	0.07 \pm 0.03	8.70 \pm 2.11
1.0	0.06 \pm 0.03	11.11 \pm 2.18
1.5	0.05 \pm 0.02	15.38 \pm 2.32
2.0	0.17 \pm 0.06	22.80 \pm 7.21

FIGURE LEGENDS

Figure 1. Protein purification of ZAG in the presence of divalent metals. (A) size-exclusion chromatography of 6.2 μM ZAG (0.2 mg/ml) in the presence of 2 mM of six metal chlorides in Hepes buffer at 0.5 ml/min, followed by 7.5 mM EDTA. The ZAG monomer eluted at 23.1 min. The red line indicates the size-exclusion chromatography run with 2 mM ZnCl_2 . (B) Non-reducing gradient 4-20% native PAGE of 6.2 μM ZAG in Hepes buffer, with additions of 2 mM metal chlorides (upper panel) and increasing concentrations of zinc chloride followed by excess EDTA (lower panel). (C, D) Dynamic light scattering of ZAG with additions of zinc and barium chlorides respectively, followed by excess EDTA.

Figure 2. Secondary and tertiary structure changes in ZAG with divalent metals. (A) UV absorbance spectra of ZAG between 240 nm-400 nm in the absence and presence of 1.8 mM metal chlorides. (B) Plot of Turbidity (apparent Absorbance) at 340 nm of ZAG with increasing concentrations of metal chloride specified in the panel. (C) Near-UV and (D) Far-UV CD spectra of ZAG in the absence and presence of 1.8 mM metal chlorides, with the buffer baseline subtracted from each sample spectrum prior to correction for the effects of dilution. All measurements were made using 6.2 μM ZAG in 10 mM Hepes, pH 7.4, in the absence of NaCl. Data highlighted using a red line indicates the presence of ZnCl_2 .

Figure 3. Sedimentation velocity of ZAG with zinc and barium chlorides. Three sedimentation data and boundary fits are shown for (A) 6.2 μM ZAG in Hepes buffer, titrated with (B) 2.0 mM zinc chloride and (C) 2.0 mM barium chloride. For clarity, only every third scan is shown in the fitted data plots. The sedimentation coefficient $c(s)$ distribution analyses of 6.2 μM ZAG titrated with (D) increasing concentrations of zinc chloride, followed by excess EDTA, and (E) increasing concentrations of barium chloride followed by excess EDTA. (F) The proportion of ZAG monomer and oligomers with increasing concentrations of zinc chloride and barium chloride. The loading concentration values were obtained by integration of the $c(s)$ distribution at 50,000 rpm. Data highlighted using a red line indicates the presence of 2 mM ZnCl_2 or 2mM BaCl_2 and green indicates the presence of excess EDTA.

Figure 4. Sedimentation velocity of the fluorescent fatty acid C_{16} -BODIPY in the presence of ZAG and zinc. The sedimentation boundary fits correspond to (A, B) 6.2 μM ZAG, 6.2 μM C_{16} BODIPY and 0.5 mM ZnCl_2 and (C, D) 6.2 μM ZAG, 6.2 μM C_{16} BODIPY and 2.0 mM ZnCl_2 in Hepes buffer. For clarity only every third scan is shown. Panels (A, C and E) represent the fluorescence-detected sedimentation velocity experiments. Panels (B, D and F) represent the absorbance detected sedimentation velocity experiments. Data highlighted using a red line indicates the presence of 2 mM ZnCl_2 .

Figure 5. X-ray scattering of ZAG with barium chloride. (A) Guinier plot of 15 μM ZAG in the presence of increasing barium chloride concentrations in Hepes buffer. (B) Guinier analyses of 15 μM ZAG in Hepes buffer in the presence of 0.5 mM barium chloride compared with the scattering curve calculated from the ZAG crystal structure. (C) Distance distribution $P(r)$ plots of ZAG with barium chloride to follow panel (A).

Figure 6. Fluorescence emission spectra of C_{11} -BODIPY and C_{16} -BODIPY with ZAG. Fluorescence emission spectra of (A) 0.03 μM C_{16} -BODIPY, (B) 0.04 μM C_{11} -BODIPY in PBS and methanol, (C) 1.11 μM C_{16} -BODIPY upon addition of 1.11 μM ZAG and (D) 0.04 μM C_{11} -BODIPY upon addition of 20 μM ZAG. $\lambda_{\text{ex}} = 488$ nm and all fluorescence measurements were corrected for the effects of dilution and Raman scattering.

Figure 7. Binding of C₁₆-BODIPY and DAUDA to ZAG in the presence of zinc. (A) Fluorescence emission spectra at the excitation wavelength $\lambda_{exc} = 488$ nm of 0.85 μ M C₁₆-BODIPY in Hepes buffer upon sequential additions of ZAG. (B) Binding curves of C₁₆-BODIPY with ZAG in Hepes buffer containing 0 mM, 0.5 mM, 1 mM, 1.5 mM and 2 mM ZnCl₂. (C) Fluorescence emission spectra at the excitation wavelength $\lambda_{ex} = 345$ nm of 0.89 μ M DAUDA in Hepes buffer upon sequential additions of ZAG. (D) Binding curves of DAUDA with ZAG in Hepes buffer containing 0 mM, 0.5 mM, 1 mM, 1.5 mM and 2 mM ZnCl₂. All fluorescence data are corrected for the effects of dilution. To account for the quenching effect of zinc on C₁₆-BODIPY and DAUDA fluorescences, data points for all binding curves were produced by subtraction of the fluorescence emission of each probe from the fluorescence emission generated upon additions of ZAG.

Figure 8. Proposed molecular association of ZAG oligomers and its effect on lipid binding in its groove. (A) Predicted ZAG monomer, dimer and trimer in the presence of zinc. (B) Surface diagram of the basal and apical surfaces of the ZAG monomer, highlighting potential zinc-binding residues Glu (red), His (blue) and Asp (green). The remaining residues are depicted in grey. (C) Three-dimensional secondary structure cartoon of the structurally-related immune class I MHC-like molecule Cd1c in complex with the pathogenic *Mycobacterium tuberculosis* lipid antigen mannosyl- β 1-phosphomycolate (blue spheres) and a C12 alkyl chain (orange spheres) (PDB code 3OV6). All images were created using PyMOL software.

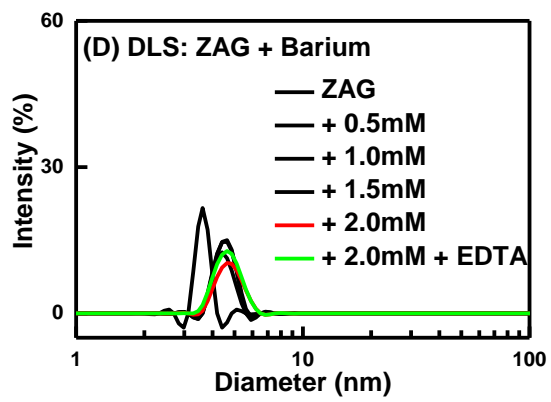
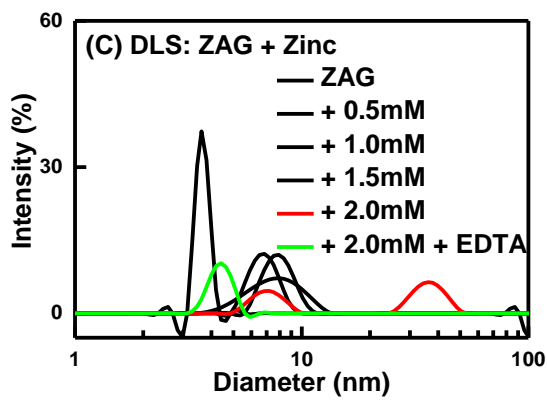
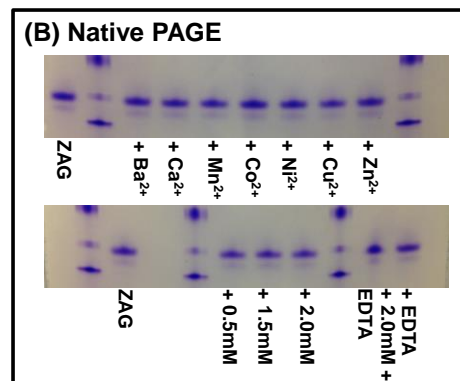
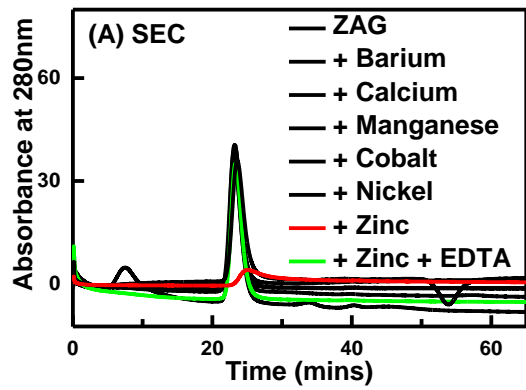


FIGURE 1

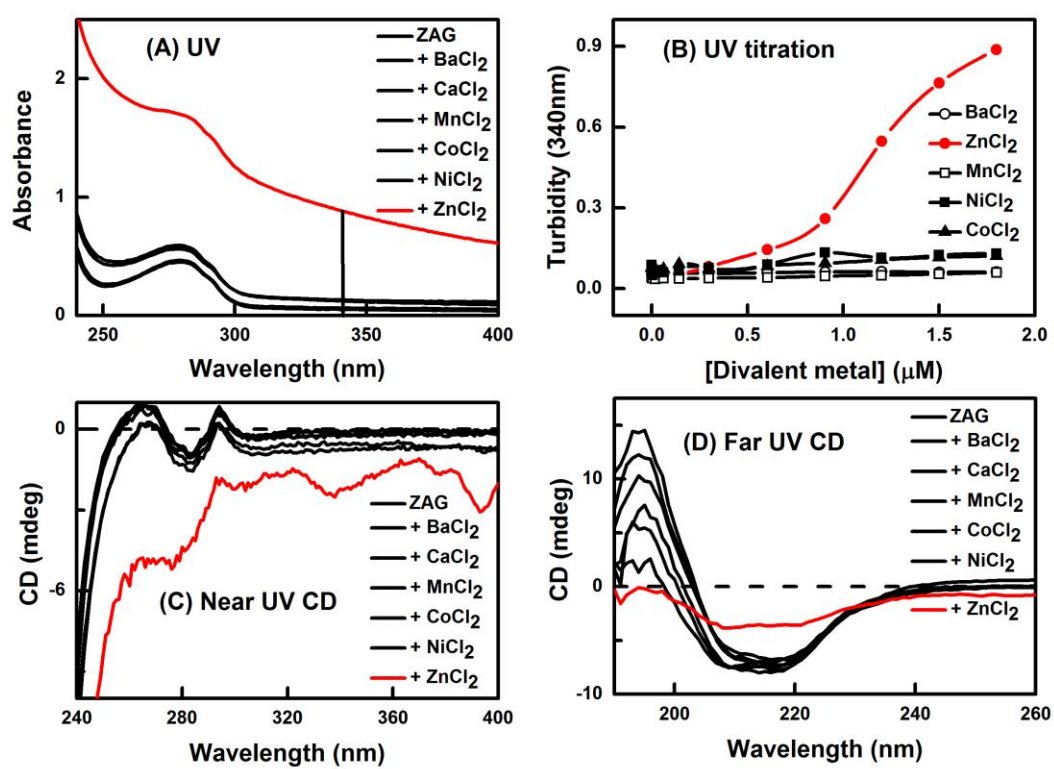


FIGURE 2

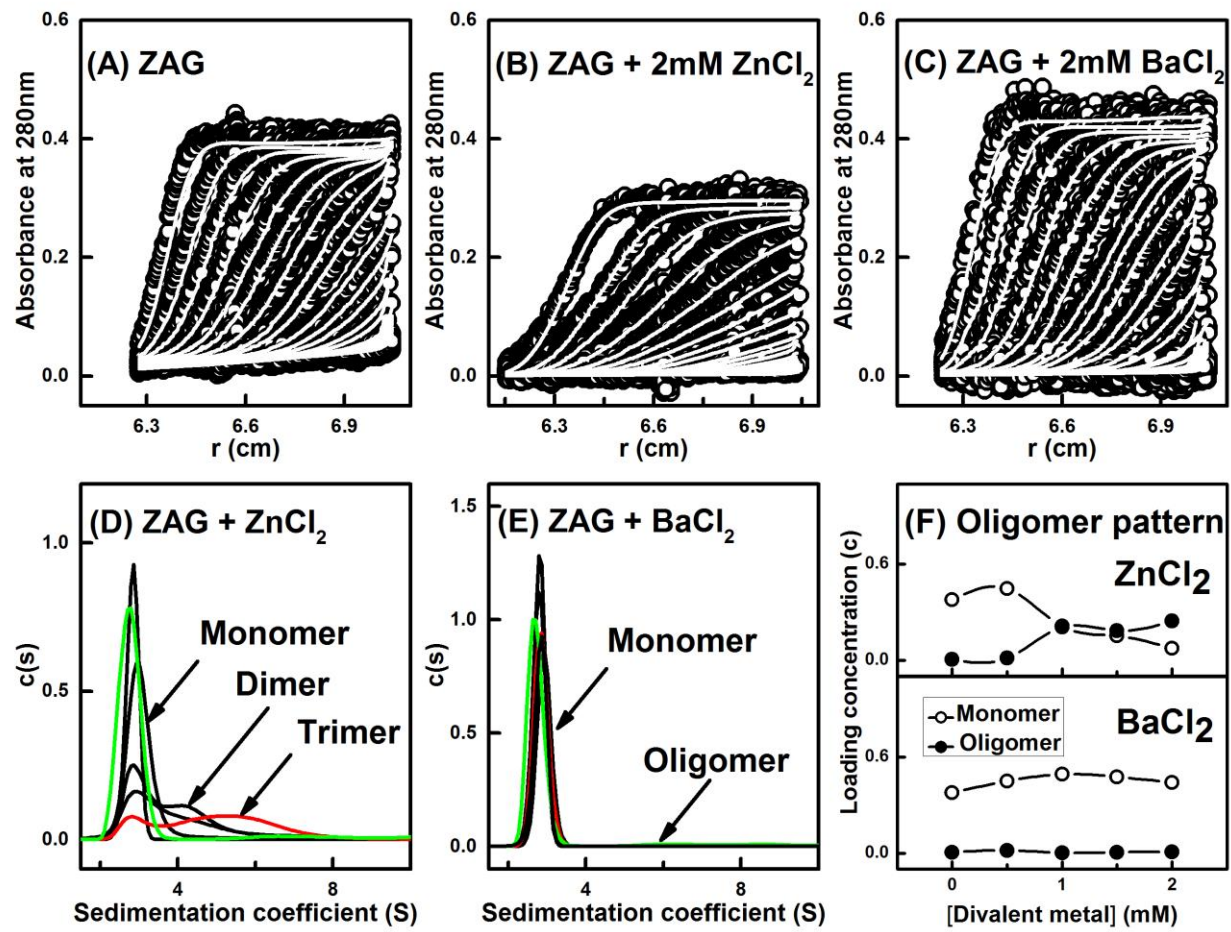


FIGURE 3

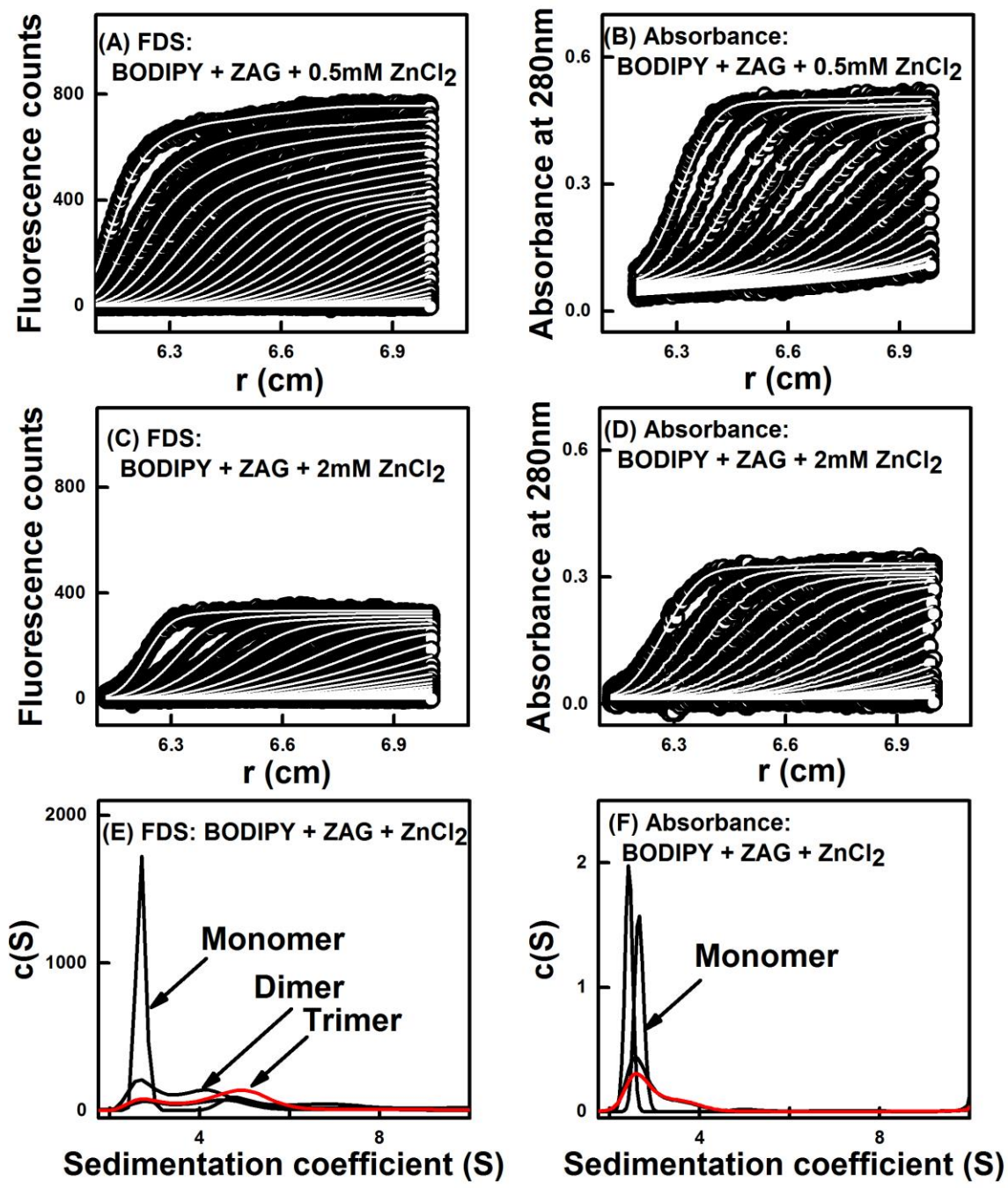


FIGURE 4

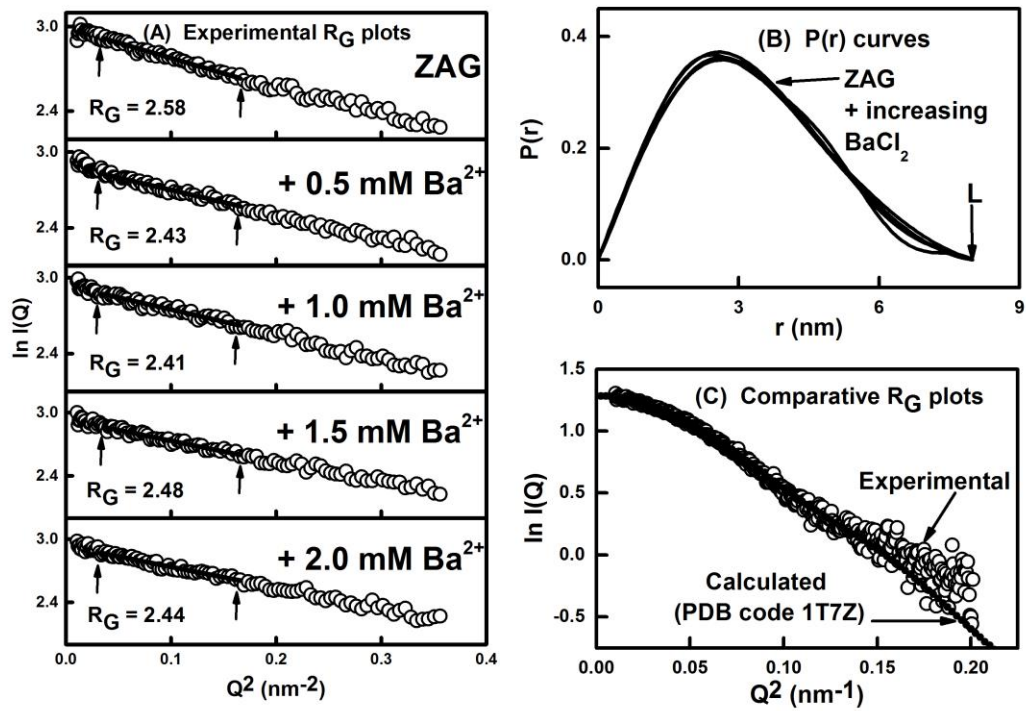


FIGURE 5

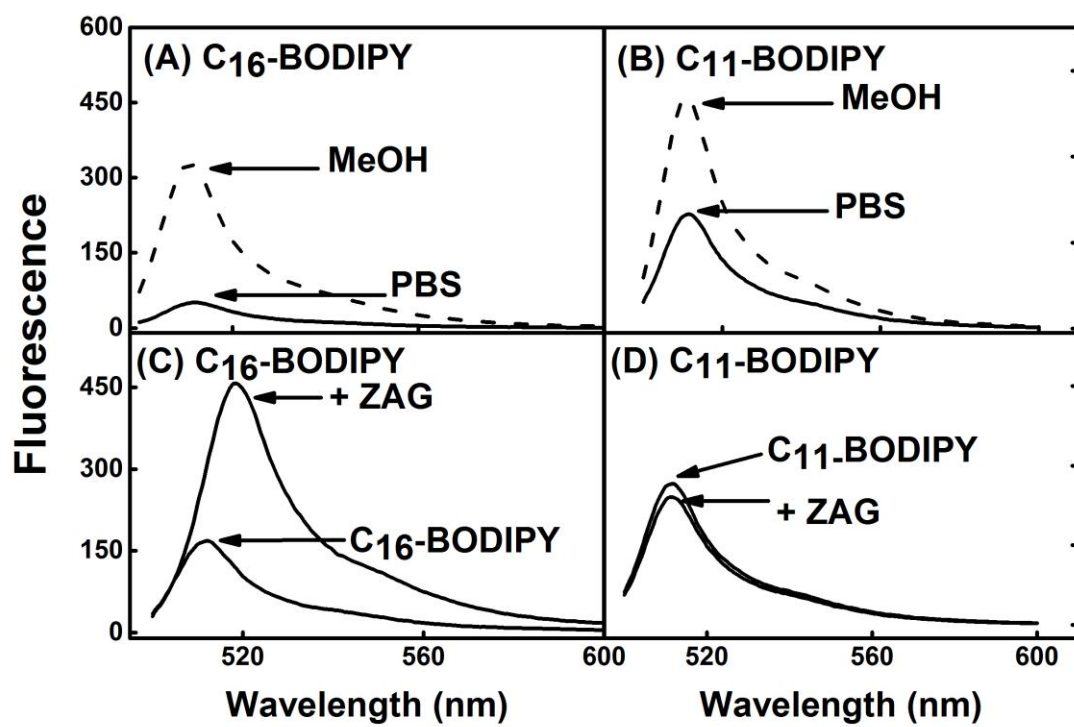


FIGURE 6

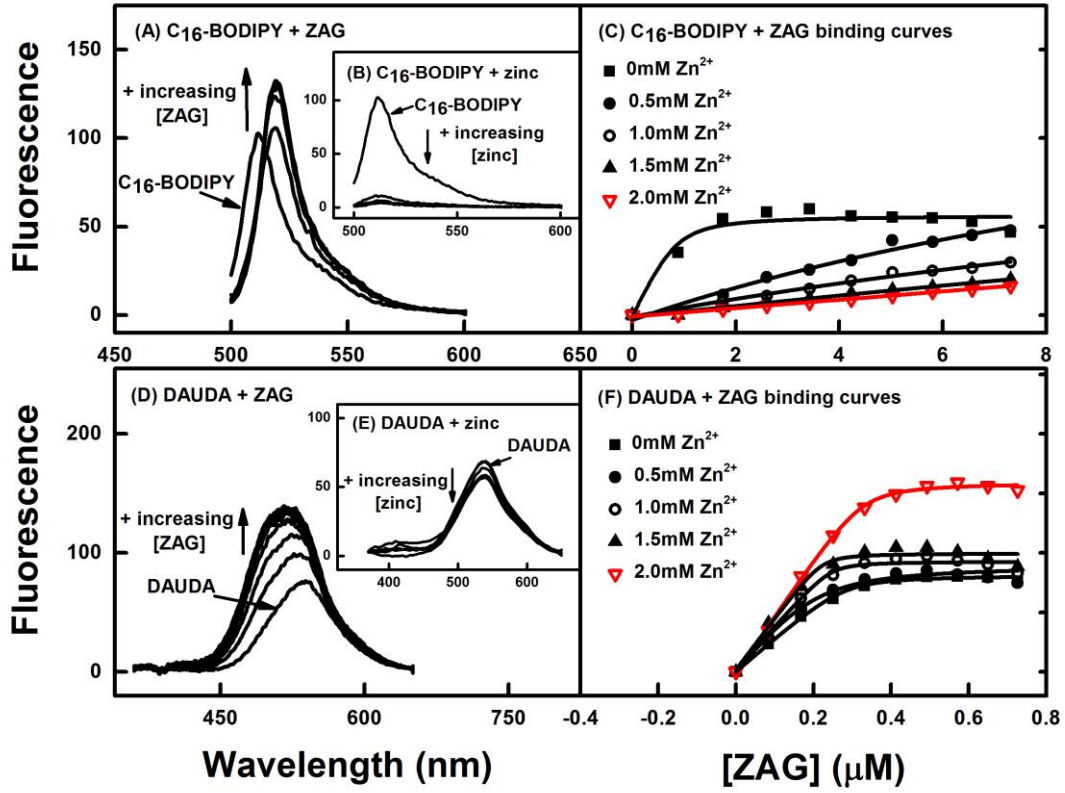


FIGURE 7

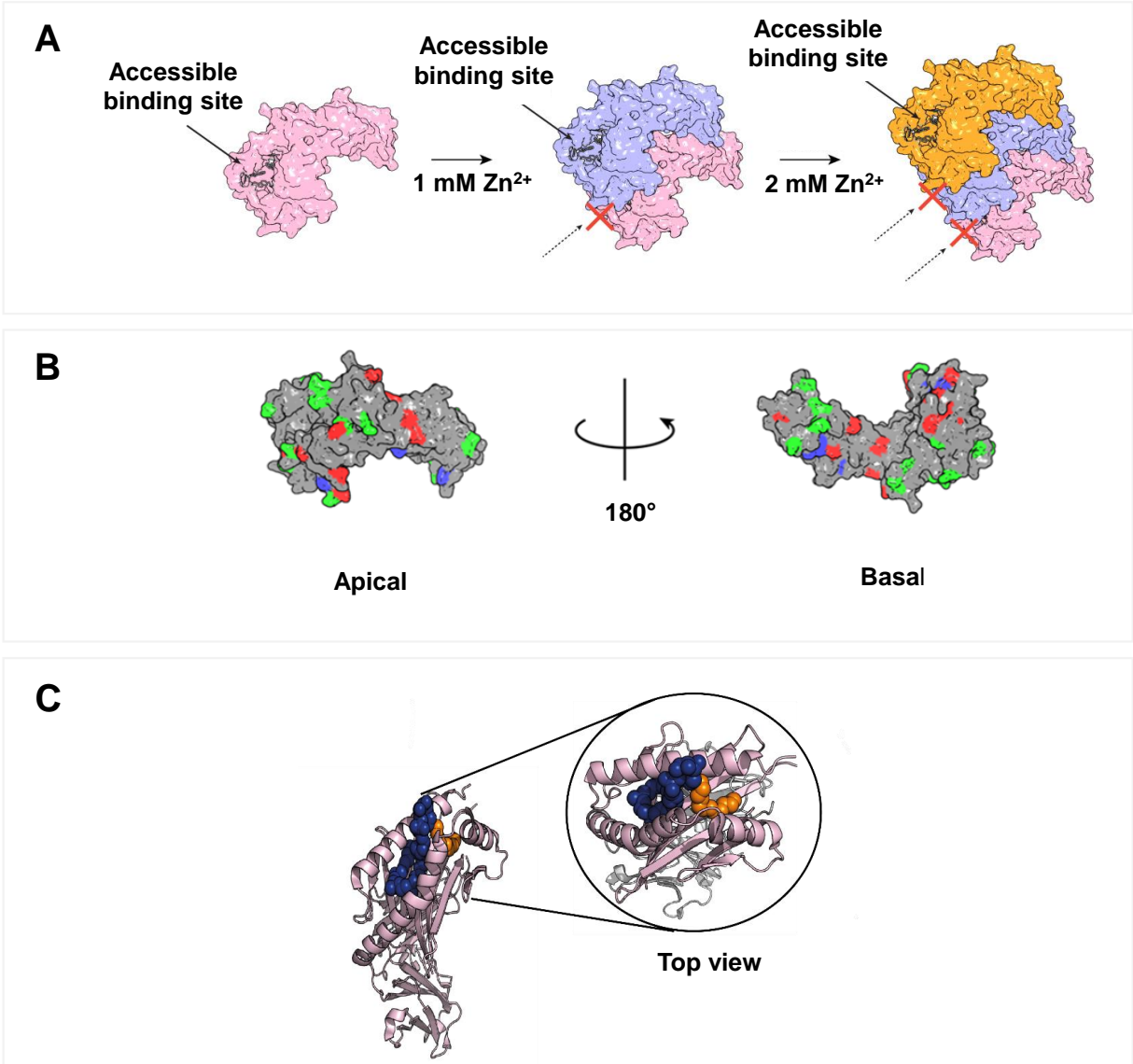


FIGURE 8